PHYSICAL REVIEW MATERIALS **7**, L080401 (2023)

Letter

Crystal to crystal transformation in soft ionic microgels: Kinetics and the role of local mechanical susceptibilities

Saswati Ganguly,[1,2,*] Sofi Nöjd,[3] Anand Yethiraj,[4] Peter Schurtenberger,[3] and Priti S. Mohanty[3,5,†]
[1]*Soft Condensed Matter Theory, Department of Physics, University of Konstanz, 78457 Konstanz, Germany*
[2]*Institute of Materials Physics in Space, German Aerospace Center (DLR), 51170 Cologne, Germany*
[3]*Division of Physical Chemistry, Lund University, P.O. Box 124, SE-22100 Lund, Sweden*
[4]*Department of Physics and Physical Oceanography, Memorial University, St. John's, Newfoundland NL A1B 3X7, Canada*
[5]*School of Chemical Technology and Biotechnology, Kalinga Institute of Industrial Technology (KIIT), Deemed to be University, Bhubaneswar 751024, India*

(Received 22 November 2022; revised 25 July 2023; accepted 1 August 2023; published 28 August 2023)

We report confocal microscopy experiments of electric-field-driven crystal-crystal transformations in microgel colloids with varying particle softness. The transformation kinetics are well described by phenomenological nucleation and growth theory. Using a spatial projection formalism, we determine local susceptibilities to affine shear deformation and nonaffine defect formation in the parent crystal. Curiously, the softer particles have lower shear strain susceptibility, while nonaffine susceptibility and phenomenological growth coefficients depend nonmonotonically on particle softness.

DOI: 10.1103/PhysRevMaterials.7.L080401

Introduction. Material properties of crystalline solids are direct functions of their microstructures. Different crystalline phases often coexist and undergo structural transformations when subjected to changing thermomechanical environments. Solid to solid structural transformations find relevance in a wide array of processes, from production of diamonds with desired strain resistance [1] to phase changes in the earth's mantle [2,3]. Properties like work hardening [4,5] and shape memory effects [6] in metals or alloys are direct consequences of crystal to crystal transitions and they have important technological implications. All these examples, however, are observed phenomenology with little clarity regarding the underlying particle level events leading to the emergence of the macroscopic properties.

Fundamental questions exist: for example, how do changing atomic interactions affect the microstructures and the resulting macroscopic phenomenology of phase transformation kinetics? One of the challenges in uncovering fundamental rules governing such processes is the extremely small length scales and timescales of atomic motions during structural transformations in metallic alloys. While recent electron microscopy experiments [7] are allowing tracking of individual particles in a mobile solid-solid interface, they are nevertheless limited to small regions near a grain boundary.

Suspensions of spherical colloidal particles have been used to obtain valuable insights into solid-solid phase transformation kinetics on the single-particle level, in two [8] and three [9] dimensions. More recently, temperature-sensitive microgel colloids have been used to examine crystal nucleation in a quasi-two-dimensional solid-solid transformation [10]. Ionic microgel colloids with confined counterions [11], soft-repulsive interactions [12], *and* electric-field-induced interactions, have been employed to investigate interesting phenomenologies at solid-solid phase transformations in three dimensions [13], including long-lived metastable states.

In statistical mechanics, one thinks in terms of a Hamiltonian connected to the interparticle interactions, which indeed can be experimentally controlled in colloids. A recent investigation [12] has demonstrated control of phase diagrams via control of the zero-field interparticle interactions in thermoresponsive ionic microgels by varying cross-linker density. There is, however, a fundamental disconnect between theory and experiment. The effective interactions in experimental systems can change *nontrivially* in ways that are hard to theoretically model across the phase diagram. As an alternative to modeling interparticle interactions, a geometric analysis of particle trajectories has been shown [14] to record profoundly different collective displacement modes in an equilibrium crystal and a crystal during phase transformation.

In this Letter, we examine the possibility of systematically modifying the transformation kinetics of a crystal-to-crystal transition through direct manipulation of both the zero-field interparticle interactions and the field-induced dipolar interaction in soft ionic microgels at varying cross-linker density. From the experimental particle configurations we obtain the population fraction of the product crystalline phase, as a function of time: the resulting distinct dependence can be fitted to a Johnson-Mehl-Avrami-Kolmogorov [15–18] model. As an independent yet complementary theoretical study, we present a framework to analyze displacement fluctuations in pretransition parent crystals to measure local mechanical susceptibilities. These properties serve as precursors to the observed transformation kinetics.

Transformation kinetics. The transformation of a face-centered-cubic (fcc) lattice transforming to a body-centered-

---

[*] Corresponding author: saswati.ganguly@uni-konstanz.de

[†] Corresponding author: pritisundar.mohanty@kiitbiotech.ac.in

tetragonal (bct) lattice, induced by an ac electric field, is studied in three separate microgels of varying cross-linker densities. For hard spheres it is already known that the fcc is the stable zero-field structure while the bct crystal is the lowest energy state for field-induced dipolar hard spheres [9,19,20]; these are also the lowest energy structures for soft microgel colloids [21]. The latter systems can be prepared with different interparticle interactions by varying cross-linker density, and are labeled as TS1.5, TS5, and TS10 for 1.5%, 5%, and 10% mole fractions, respectively.

The dynamics are obtained from image series obtained around 10 particle diameters away from the bounding surface to minimize surface effects. Quasi-two-dimensional particle dynamics are recorded during the transformation by keeping the [001] lattice axis of the fcc and bct crystals, aligned along the direction of the electric field. Therefore, the fcc to bct transformation is perceived as a transformation of a 2D triangular phase to a square lattice structure, as shown in previous work [9,21].

The experimental electric-field setup is similar to previous experiments reported in Refs. [22] and [13]. In order to maintain a homogeneous ac electric field across the sample, the microgel suspension is kept between two indium-tin-oxide-coated transparent coverslips separated by 120 μm spacers and the ac electric field is applied along the Z direction and imaging is done in the XY plane.

Earlier ac electric field studies [21,23] on soft ionic microgels demonstrated a tendency to form chains via self-assembly on decreasing the frequency from 1.5 MHz to 100 kHz at constant field strength. This frequency-dependent field-driven assembly is understood from dielectric studies [11] explaining the particle-polarization mechanism at different frequency regimes. In the low-frequency regime (below 10 kHz), the polarization is due to the mobility of internal counterions; at an intermediate-frequency regime (∼10 to 100 kHz), the polarization is governed by a diffuse double layer around the particles; in the high-frequency regime (∼ MHz), the polarization is due to the polymer backbone. It is also observed that the polymer backbone polarization is much weaker compared to double-layer and counterion polarization arising at low and intermediate frequencies. For finite electrode gap widths, the additional contributions from electrode polarization effects become dominant at low frequency ($\ll$100 kHz). To be on the safer side, all our ac electric field experiments presented in this Letter are at a fixed frequency of 100 kHz.

The ac field-induced interparticle interactions among ionic microgels have been explicitly explained in a recent work [23] by some of the authors. Using a theoretical coarse-graining approach, it has been depicted that the contributions to an effective pair potential for our system of ionic microgels include electrostatic (monopole-monopole and partially screened dipole-dipole) interactions as well as a short-ranged soft, repulsive interaction for distances shorter than the particle diameter. The structural properties (pair-correlation function) of 5 mol % cross-linked microgels derived from the electric field experiments are very well reproduced by these theoretical models in fluid and fluid-string regions of the phase diagram. In the current case, we use a similar system of PNIPAM-co-PAA ionic microgels, but with varying cross-linker densities. We thus expect an analogous theoretical approach to describe the structural properties of microgels for different cross-linker densities if the theoretical models incorporate the required input parameters from the experiments in fluid and fluid-string regions of the phase diagram. It is to be noted, however, that these [23] theory and simulation studies are restricted to fluid and fluid-string regions of the phase diagram. Therefore, the predictive power of the theoretical models requires further investigation before they can be employed in studying the various self-assembly scenarios leading to ordered structures such as the ones presented in this Letter.

Our experiments are carried out in the swollen state of poly(N-isopropylacrylamide-co-acrylic acid) microgels at 20 °C. The effective volume fractions of initial zero-field fcc crystalline samples, $\phi_{\text{eff}} = 1.47$ (TS1.5), 1.39 (TS5), 0.96 (TS10), are above the close-packed volume fraction, ϕ_{cp}, where the particles overlap and lead to a soft-repulsive interaction that varies for different cross-linker density [12]. Refer to the Supplemental Material [24] for details of synthesis parameters, particle properties, and the experimental setup for the confocal microscopy studies in an ac electric field.

The transformation kinetics of TS5 and TS10 are discussed first. Both these systems exhibit the transformation when the system is subjected to constant electric field strengths of 0.104 V/μm and 0.12 V/μm, respectively. TS1.5 has the lowest cross-linker density at 1.5 mol % and is expected [12] to have the softest interparticle interaction. This system requires a ramping of the electric field from 0.058 V/μm to 0.116 V/μm. Unlike TS5 and TS10, the structural transformation in this case never reaches completion in the presence of a single constantly held electric field. Therefore, the kinetics of this system are discussed as a separate case study.

The phase transformation trajectories are tracked by measuring the decrease in the fraction of colloidal particles with triangular crystalline order (f_6) and the consequent increase in the fraction (f_4) of square lattice structure. The bond orientation order parameters used for this purpose are defined as $\psi_{s=4/6} = |\frac{1}{N_b}\sum_1^{N_b} e^{is\theta j}|$ with s either 4 or 6. N_b are the neighbors within the nearest-neighbor shell identified using the first peak position in the radial distribution function calculated from the quiescent fcc phases of the respective systems. θ_j is the angle between the line connecting a nearest neighbor to a lattice point and a reference axis.

We choose Johnson-Mehl-Avrami-Kolmogorov [15–18] equations with the generic form representing the decay [Eq. (1b)] of the parent phase while the product crystalline phase grows [Eq. (1a)]:

$$f_4(t) = A[1 - \exp(-Ct^{\alpha})], \tag{1a}$$

$$f_6(t) = A[\exp(-Ct^{\alpha})]. \tag{1b}$$

The decay of the parent fcc phase is seen in the time (t) evolution of the particle fraction $f_6(t)$. The growth in the bct phase, with time, is quantified through the change in the particle fraction $f_4(t)$ and is fitted to the time-dependent growth curve in Eq. (1a). Both these transformation kinetics, for our systems of interest, are presented in Fig. 1.

The Johnson-Mehl-Avrami-Kolmogorov (JMAK) [15–18] growth equations were derived to represent phase transformation kinetics involving nucleation and growth of crystals

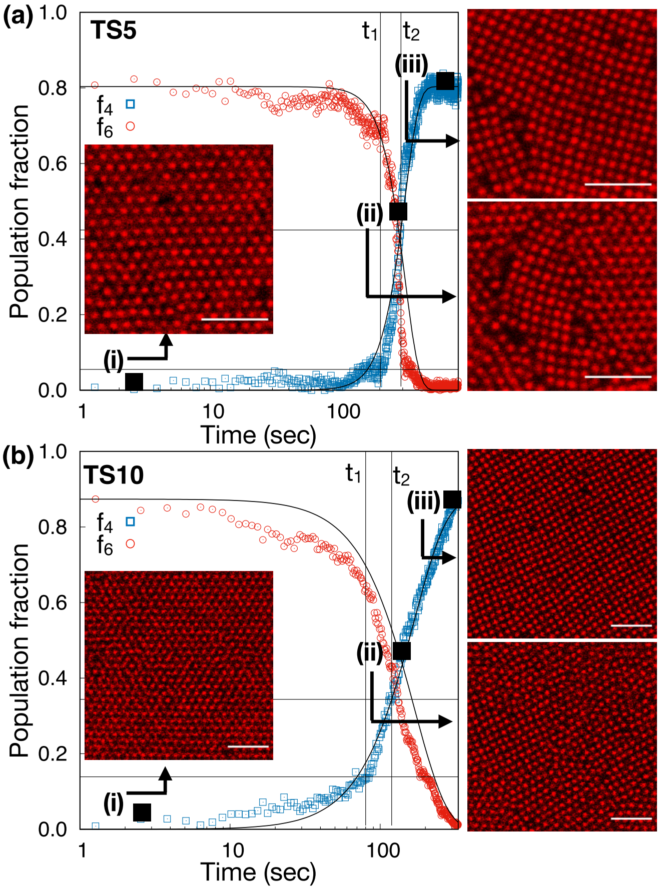

FIG. 1. (a) Plots of the population fraction f_4 (blue square symbols) and f_6 (red circle symbols) as they evolve with time during the fcc to bct transition for the system TS5. f_4 is fitted to a function of the form $A[1 - \exp(-Ct^4)]$ given in Eq. (1a) and shown by the black $\mathcal{S}$ curve through the data points of f_4. The black curve through f_6 represents the corresponding decay curve from Eq. (1b). The times t_1, t_2 and their respective $f_4(t_1)$, $f_4(t_2)$ are indicated by straight lines. Black squares denoted by (i), (ii), (iii) on the growth curves correspond to time points for the colloidal configurations given here. In each snapshot, the single white line denotes length scale of 10 μm. (b) Plots of the population fractions f_4 and f_6 for the system TS10. f_4 is fitted to a function of the form $A[1 - \exp(-Ct^2)]$. The symbols have meanings identical to those in the case of TS5.

from liquids or one crystalline solid from another crystalline solid. These equations have been widely used and modified to study crystallisation processes in metals, alloys, and colloidal crystals [25]. These models rely on phenomenological parameters obtained through fitting the mathematical function to actual experimental measurements. Such models on the other hand find some statistical thermodynamics basis when theoretical interpretations or atomistic simulations describe the phenomenological parameters in terms of familiar thermodynamic free energies in models with the classical many-body Hamiltonian [26].

The original formulation of the JMAK equations provides important insights in understanding the crystal to crystal structural transition despite the various sources of deviations from the assumptions [24] made in deriving them. They identify two key contributions [27–29] to the time dependence of the transformation kinetics: (i) the nucleation rate (K_n) of the product phase within the parent phase, and (ii) the growth rate (K_g) of the nuclei governed by the mechanisms of transport processes in the elastic medium. Substituting $A = 1$, $\alpha = 4$, $C = \frac{\pi}{3} K_n K_g^3$ in Eq. (1a) gives standard random nucleation and homogeneous growth kinetics for a three-dimensional system (see Supplemental Material [24] and Refs. [30,31] therein).

TABLE I. Nonmonotonic dependence on cross-linker density: The table enlists the change in bond order parameters $f_4(t_2) - f_4(t_1)$ across the time windows $(t_2 - t_1)$, the coefficients α [see Eq. (1a)], and the nonaffine susceptibilities $\langle \chi^2 \rangle - \langle \chi \rangle^2$ [see Fig. 3(c)] for the three systems. All these three quantities change nonmonotonically as the cross-linker densities are increased.

System	$[f_4(t_2) - f_4(t_1)]/(t_2 - t_1)$ (sec^{-1})	α	$\langle \chi^2 \rangle - \langle \chi \rangle^2$
TS1.5	$0.16/10.8 = 14.81 \times 10^{-3}$	2.1	75.98
TS5	$0.37/88.3 = 4.19 \times 10^{-3}$	4.0	138.78
TS10	$0.21/39.3 = 5.34 \times 10^{-3}$	2.0	18.84

In Fig. 1 we present our experimentally observed growth in the population fraction f_4 of the bct phase while the volume fraction of the fcc phase decays. Figure 1(a) shows the transformation kinetics for the system TS5 in the presence of an electric field strength of 0.104 V/μm. In this case we first fit the resulting growth curve to a JMAK equation of the form given in Eq. (1a) with $\alpha = 4$. This is consistent with the similar experimental results reported in a previous contribution [13] by some of the authors. The constant A is chosen to reflect the maximum population fraction of the product phase which, in the case of TS5, is ≈0.8. The constant C is obtained through a nonlinear least-squares fitting of the time-dependent function in Eq. (1a). We use the same set of constants in the decay curve given in Eq. (1b) and then compare this to the decrease in the population fraction of the fcc phase shown by the red symbols in Fig. 1(a). The reasonably good fit to the decay curve of the fcc phase indicates that the parent phase transforms to the product phase with very little time lag. This concurrence in the decay of fcc and growth of bct in our experiments is different from similar structural transformation scenarios [10] induced using temperature change. Differentiating the growth equation [Eq. (1a)] with respect to time helps one extract a characteristic timescale $t_2 = [(\alpha - 1)/\alpha C]^{1/\alpha}$ indicated by the maxima in the derivative of the growth function in Fig. 1(a). This is preceded by another point t_1, the experimental induction time, where the curve shows a sudden rise. The point is determined by taking the intersection of lines fitted to the initial flat region of data points for $f_4(t)$ and the subsequent steeper region of the curve. The difference $(t_2 - t_1)$ and the fraction of the product phase formed in that time window, for all three systems, are compared in Table I.

An analysis, identical to the one for the system TS5, is repeated for TS10 with much higher cross-linker density. In this case, the threshold field strength required for the onset of the transformation is 0.12 V/μm. The results of this analysis are presented in Fig. 1(b). A growth curve [Eq. (1a)] with time exponent $\alpha = 2$ signals a transformation kinetics distinct from the nucleation and growth scenario exhibited by the system TS5.

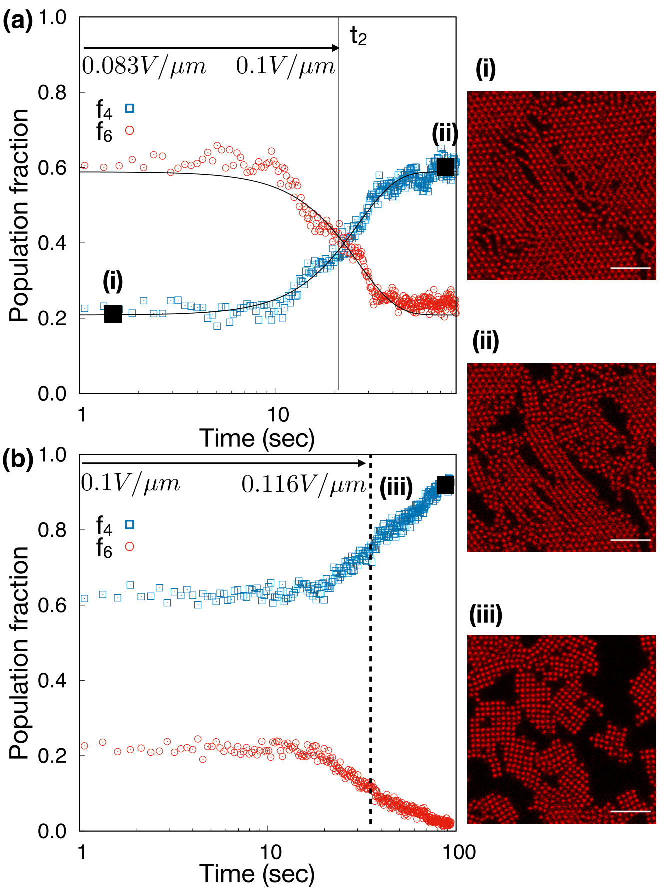

FIG. 2. Plots of population fractions f_4 (blue squares) and f_6 (red circles) as they evolve with time during the fcc to bct transition for the system TS1.5. Unlike in the case of TS5 and TS10, for the system TS1.5 the complete transformation happens in stages. After an initial arrest in the transformation at a population fraction of ≈0.2 the transformation commences on increasing the field magnitude. (a) The field strength is increased from 0.083 V/µm to 0.1 V/µm thus leading to 0.6 population fraction of the product phase. f_4 is fitted to a function of the form $A[1 - \exp(-Ct^{2.1})]$ and is represented by the black line. (b) Plots of f_4 and f_6 as a smooth increase in the field strength from 0.1 V/µm to 0.116 V/µm leads to completion of the transformation process. Black squares indicate the times corresponding to the configurations (i), (ii), and (iii). The white lines in the snapshots denote length scale of 10 µm.

The system with the lowest cross-linker density TS1.5 exhibits transformation kinetics different from either TS5 or TS10. In this case, an initial electric field of 0.058 V/µm only leads to a very small volume fraction of ≈0.2 of the product phase. Multiple trials of the experiment at the constant electric field held at various values ranging from 0.058 to 0.116 V/µm results in similar saturation of the product phase at small volume fractions. The only successful experimentally attainable protocol to bring about the structural transformation occurs when the system is subjected to a slow ramping of the electric field. Figure 2(a) shows one such scenario where initially the electric field is increased from 0.083 to 0.1 V/µm within a time window of 22 seconds. The field is then held constant to observe the growth of the product phase. However, unlike either TS5 or TS10, the growth of the product phase, once again, gets arrested at ≈0.6 population fraction. At this point, the field is turned on again and slowly increased from 0.1 to 0.116 V/µm within a window of 35 seconds. This ultimately ensures the completion of the structural transformation. The configurations of the product phase (see Fig. 2) in this system exhibit clustering of particles with the square-lattice structure while leaving voids at other regions. This is attributed to particularly strong interpenetration of the microgels in the presence of the external field. When compared to the systems TS5 and TS10, this may have a greater impact on the morphology of the colloidal chains along the z direction. Future studies, equipped to accurately study the 3D particle kinetics, will provide better insights regarding these nuanced aspects already indicated in the current quasi-2D experiments.

Even if a different protocol is required for the completion of the structural transformation in case of TS1.5, here once again we compare the growth curve shown in Fig. 2(a) to the JMAK relation Eq. (1a), and extract values for the parameters $\alpha = 2.1$ and $(t_2 - t_1) = 10.8$ seconds (see Table I). The well-defined threshold field strengths for the onset of transformation in TS5, TS10 and the unique transformation protocol for TS1.5 are repeatedly observed in experiments performed with independently prepared samples. The parameters associated with the transformation kinetics are reproduced in such reruns of the experiments.

The quiescent phase before transformation. Now we have established the distinct transformation kinetics of the fcc to bct phase, using the JMAK coefficients, when colloidal interactions are modified through change in the cross-linker density. A previous study [12] exploring the phase behavior of thermoresponsive microgels shows that lower cross-linker density translate to softer interactions through larger hydrodynamic radii and longer dangling ends. Here, we present a spatial-projection operator [32,34] based analysis of the 2D cross sections of the quiescent parent crystalline phase. This allows us to obtain (i) susceptibilities of affine particle displacements leading to formation of rectangular unit cells from a triangular unit cell [see the second inset of Fig. 3(b)] and (ii) susceptibilities for the formation of defects which are expected to show up at the interface (see Supplemental Material [24]) as a product crystalline phase forms and grows within a parent lattice structure. The kinetics of a phase transformation, involving nucleation and growth, are dictated by two free energy contributions: (i) the gain in energy due to the formation of the second phase within the first and (ii) the energy cost due to the formation of an interface between the phases. The susceptibilities mentioned above give us access to the propensity of nucleation and growth even when explicit theoretical evaluation of the free energies is not possible due to lack of an appropriate model for the interparticle interactions. In our specific example of a triangular lattice transforming to a square, an affine shear mode [see inset in Fig. 3(b)] transforms a triangular unit cell to a square. On the other hand, defects form at the interface of the nucleated square lattice and the parent triangular network (see Supplemental Material [24] for a schematic diagram). The nonaffine parameter is known to mark particle neighbourhoods with lattice defects, and complementary affine deformations mark uniformly sheared regions. Therefore, our subsequent analysis presumes a connection between nucleation/growth and affine/nonaffine

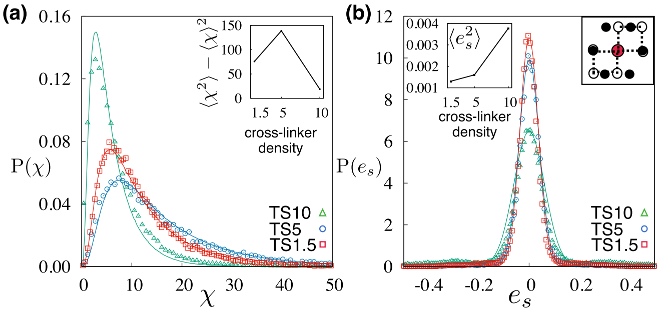

FIG. 3. (a) Plots of the probability distributions of the nonaffine parameter $P(\chi)$ for the systems TS1.5, TS5, and TS10. The open symbols represent the $P(\chi)$ obtained from the experimental data. The lines show χ^2 distributions of degree 8, fitted to the experimental data. The inset shows the second moment $(\langle\chi^2\rangle - \langle\chi\rangle^2)$ as a function of the cross-linker densities for the three systems. (b) Plots of the probability distribution functions for the local shear strain $P(e_s)$. The symbols have the same meaning as in (a). The lines show Gaussian distributions fitted to the experimental data. The first inset (top left) shows the second moments $\langle e_s^2\rangle$ of the distributions $P(e_s)$. The second inset (top right) shows a single triangular unit cell with black filled circles. The open circles show the same unit cell after an affine shear strain.

deformations in the context of crystal to crystal structural transformation.

Particle displacements obtained by optical microscopy allow this analysis within a theoretical statistical mechanics framework. References [32] and [14] developed a projection operator formalism for atomic displacements in solids such that collective modes within a predefined coarse-graining volume Ω that originate from affine displacements (like shear) of the particles can be separated from nonaffine displacement fluctuations. In order to obtain the nonaffine parameter χ and the best-fit affine strain $\mathbf{e}$, for neighborhood Ω of a particle, one needs to minimize the function

$$\chi = \min_{\mathbf{e}}[\Delta - R\mathbf{e}]^2, \tag{2}$$

thus maximizing $\mathbf{e}$. This results in the expressions for χ and $\mathbf{e}$

$$\chi = \Delta P \Delta, \text{ with } \; P = I - RQ, \tag{3}$$

$$\mathbf{e} = Q\Delta, \text{ where } \; Q = (R^T R)^{-1} R^T, \tag{4}$$

in the form of projections of the displacement Δ by the projector P constructed from the reference R.

The nonaffine parameter χ, with the dimension of $(\text{length})^2$, is a sum over the eigenvalues of a matrix PCP derived from the covariance matrix $C = \langle\Delta^T\Delta\rangle$ [32]. In Ref. [33–36] it has been rigorously shown how the eigenvectors of the matrix PCP represent thermally induced local nonaffine displacement modes associated with defect precursors in crystalline solids in two and three dimensions. This is consistent with an alternative definition [37–39] of the nonaffine parameter which associates mechanically unbalanced nonaffine forces with noncentrosymmetric local regions in materials and hence provides a connection to indentation-induced breaking of local centrosymmetry leading to dislocation formation in metals [40]. More recently, explicit connections have been made [41] between local nonaffine susceptibilities $(\langle\chi^2\rangle - \langle\chi\rangle^2)$ and binding sites in proteins. From our previous study [14], we know that the nonaffine parameter is sensitive in identifying difficult-to-detect particle rearrangements and defects in colloidal crystal configurations. This geometric argument is reiterated in the Supplemental Material [24] with the help of a schematic.

As illustrated in the inset of Fig. 3(b), an affine shear of the nearest neighborhood Ω can transform a triangular unit cell to a rectangular one. It is also one of the thermally excited affine eigenvectors of the matrix $(I - P)C(I - P)$ within our spatial projection formalism [32]. Thus, the affine shear mode is a precursor to nucleation of a square lattice (2D cross section of bct) within a triangular lattice (2D cross section of fcc).

Within the linear response picture [42], a small change in a thermodynamic variable (like strain) in response to an external field can be written in terms of equilibrium fluctuations in the thermodynamic variable in the absence of the field. As an example, consider the strain response $\langle e_s\rangle_\Sigma$ in the thermodynamic limit to a small uniform stress Σ. Linear response implies

$$\langle e_s\rangle_\Sigma = \langle e_s^2\rangle_{\Sigma=0}\Sigma, \tag{5}$$

where $\langle e_s^2\rangle_{\Sigma=0}$ is the strain fluctuation in absence of the stress field Σ and is also equal to $(\text{elastic constant})^{-1}$.

In the case of our field-induced fcc to bct transformation, the affine strain $\langle e_s\rangle$ and the nonaffine parameter $\langle\chi\rangle$ are treated as similar local response functions [34]. Therefore their second moments $\langle e_s^2\rangle$ and $\langle\chi^2\rangle - \langle\chi\rangle^2$, measured in the quiescent crystals, represent susceptibilities to respective particle displacement modes.

Given this background, here we postulate that the affine susceptibility $\langle e_s^2\rangle$ can be a strong indicator for the ease of nucleation of the product phase. Once a nucleus of the product phase forms within the matrix of the parent phase, the interface between the two phases is marked by defects. These interfaces are also marked by their large nonaffine parameters (see Supplemental Material [24]) which grows with the area of the interface. Therefore a nucleus of the product phase can be expected to grow with greater ease in a parent phase with higher nonaffine susceptibilities $(\langle\chi^2\rangle - \langle\chi\rangle^2)$ that relates to ease of defect formation.

The fcc to bct structural transformation scenarios presented here are induced in the fcc phase only after the system is subjected to a threshold magnitude of electric field. For each system, we analyze 50 configurations of the quiescent parent phase in the presence of the electric field. The per-particle nonaffine parameter χ [see Eq. (3)] and the component of the local shear strain e_s [see Eq. (4)] are calculated from colloidal particle coordinates, following procedures identical to the description given in Ref. [14]. We are working with three different systems with equilibrium nearest-neighbor distances r_0 obtained from their radial distribution functions in the quiescent crystalline phase. So we scale the calculated χ values with the respective r_0^2s for the systems TS1.5, TS5, and TS10 to make them dimensionless. As e_s is a ratio between lengths, it is a dimensionless quantity with values ranging from −1 to 1.

After obtaining the per-particle χ and e_s from the experimental data, we calculate their probability distribution functions. For an undeformed crystalline solid at a finite temperature, the probability distribution of χ is a χ^2 distribution [14,32] and the probability distribution of the affine shear e_s is a Gaussian distribution with zero mean [32]. Therefore, comparing them to these well-defined distribution functions allows us to accurately estimate the nonaffine susceptibilities $(\langle \chi^2 \rangle - \langle \chi \rangle^2)$ and local shear strain susceptibility $\langle e_s^2 \rangle$ [see Fig. 3(c)]. The excellent agreement of our experimental probability distributions with theoretical predictions consistent with a harmonic approximation reiterates previous assertions [14,43] regarding the harmonic nature of thermalized colloidal crystals.

Discussion and conclusions. Figure 3, which plots probability distributions for the nonaffine parameter and the local shear strain for three different cross-linker densities (TS1.5, TS5, and TS10 in order of increasing cross-linker density and thus decreasing softness), highlights two key results in this work. The probability distribution functions $P(e_s)$ presented in Fig. 3(b) show a systematic increase in the variance of the Gaussians for systems with higher cross-linker density. This is quantified as the second moment $\langle e_s^2 \rangle$ of the local shear strain, shown in the first inset of Fig. 3(b). Note how the figure in the inset of Fig. 3(b) represents the transformation of a triangular unit cell to a square unit cell. This is analogous to a nucleation event of a square lattice within a triangular network. A schematic diagram in the Supplemental Material [24] shows the increase in the local shear strain e_s at the central particle due to this displacement mode. Since the quantity $\langle e_s^2 \rangle$ is the susceptibility of this affine shear mode, this quantity can be representative of the ease of nucleation of the product phase within the parent lattice. Here the system TS10 appears to have the highest nucleation susceptibility while TS1.5 appears to have the lowest nucleation susceptibility. This quantity $\langle e_s^2 \rangle$, representing the elastic compliance (see Eq. (5) and [44]) of a local shear mode [see inset of Fig. 3(b)], suggests an increase in the local stiffness with decrease in the cross-linker density. This is a surprising result.

From previous studies [12] in the absence of an electric field, one expects a lower bulk modulus for systems with lower cross-linker densities. Our local shear strain compliance $\langle e_s^2 \rangle$ shows a completely opposite trend. However, this can be explained by noting the clearly perceptible [12] longer dangling ends leading to resistance to any cooperative particle modes in the systems with lower cross-linker densities. The constant arrest in transformation (see Fig. 2) in the case of TS1.5 finds more quantitative grounds in these parameters.

Figure 3(a), on the other hand, shows the probability distribution function $P(\chi)$ of the nonaffine parameter χ. As is evident from the distributions, the second moments $(\langle \chi^2 \rangle - \langle \chi \rangle^2)$ of χ do not show a monotonic dependence on the cross-linker densities. The plot in the inset of Fig. 3(a) shows that the system TS10 has the lowest nonaffine susceptibilities while the system TS5 has the highest. Through its connection to defects [34], nonaffine susceptibilities relate to the ease of growth of the product nuclei through the ease of formation of defect precursors. Refer to the Supplemental Material [24] for a schematic diagram showing the high magnitude of the nonaffine parameter χ at the interface of the lattice structure. This would mean that in the system TS5, the product nuclei would experience the lowest resistance to growth. The JMAK coefficient $\alpha = 4$ in this system implies a simultaneous homogeneous nucleation ($\propto t$) and spherical growth ($\propto t^3$) of the product phase. Comparing this to the case of TS1.5 and TS10 shows that these systems have a greater resistance to growth of the interface. This is reflected in the JMAK coefficient $\alpha(\text{TS5}) = 2$ and $\alpha(\text{TS1.5}) = 2.1$, respectively. The parameter $\alpha < 3$ clearly points to [17] anisotropic growth of the product phase. This is another important finding of this Letter.

The system TS5, exhibiting the highest susceptibility to defect formation in its quiescent state, is also the only system with a growth curve [see Fig. 1(a)] consistent with a homogeneous nucleation and isotropic growth scenario. Moreover, the system TS10, with the lowest $(\langle \chi^2 \rangle - \langle \chi \rangle^2)$ and the hardest particles, presents opportunities for interesting future investigations in the context of theoretical studies that show examples of harder particle interactions with lower defect concentrations [45–47].

Next, we refocus on all the macroscopic as well as microscopic parameters that exhibit a clear nonmonotonic behavior with a systematic decrease in the cross-linker densities. By documenting the change in population fraction $f_4(t_2) - f_4(t_1)$ of the product phase within the time window $t_2 - t_1$ (see Fig. 1 and Fig. 2), we report a characteristic rate $f_4(t_2) - f_4(t_1)/(t_2 - t_1)$ in Table I. This rate appears to be the highest for the system TS1.5 with the lowest cross-linker density but it is smallest for the system TS5. The JMAK coefficient α [Eq. (1a)] shows a similar nonmonotonic behavior (see Table I). While it clearly suggests distinct transformation kinetics in terms of nucleation morphology and growth rates, our phenomenological interpretation is limited in providing more explicit quantitative basis for these quantities. The second and third columns in Table I report macroscopic quantities measured during the structural transition. The final column in Table I is a quantity with a microscopic origin measured before the beginning of the transition from the quiescent crystalline phase. All of them show a clear nonmonotonic behavior with the change in the cross-linker densities.

The explicit deviations of these various quantities from a monotonic dependence on the colloidal cross-linker density, often used [12] as a synonym for particle softness, highlights the necessity of a more systematic evaluation of such notions of modeling microscopic interactions. It also demonstrates the rich variety of phase behavior that can be studied using such model systems and microscopic statistical analysis tools.

Modeling [23] or manipulating [48] material properties of soft colloidal crystals require creative experiments and hierarchies of theoretical calculations with approximations. Therefore, connecting observations in colloidal experiments to fundamental concepts of microstate probabilities or free energies becomes challenging. An experimental system with a high degree of control over the phase transformation kinetics and a tool to derive important microstructural insights from the parent phase *before* the onset of the transition can therefore serve as an essential starting point for future endeavours. Future work could also focus on true 3-dimensional particle kinetics, rather than the quasi-2D kinetics which were feasible in this study. Our experiments present an approach of inducing distinct phase transformation kinetics in crystals through effective intervention at the level of interparticle interactions. Moreover, our analysis of fluctuations in colloidal particle positions, without any reference to detailed particle interactions, circumvents the conceptual difficulties of modeling interaction.

Acknowledgments. We acknowledge inspiring discussions with Surajit Sengupta. Discussions with Matthias Fuchs are gratefully acknowledged. S.G. acknowledges support from Deutsche Forschungsgemeinschaft through Grant No. FU 309/11-1, partial funding within SFB 1432 (ID 425217212) in Project No. C06, and a Zukunftskolleg independent research grant from the University of Konstanz. P.S. acknowledges financial support from the Knut and Alice Wallenberg Foundation (Project Grant No. KAW2014.0052), the European Research Council (Grant No. ERC-339678-COMPASS), and the Swedish Research Council VR (Grant No. 2018-04627). P.S.M. acknowledges support from Science & Engineering Research Board (SERB), Department of Science and Technology, India (Grant No. CRG/2020/003086), and International Cooperation Division, Department of Science and Technology, India (Grant No. DST/INT/JSPS/P-341/2021). A.Y. acknowledges support from the National Science and Engineering Research Council of Canada (NSERC, RGPIN-2019-04970).

P.S.M., P.S., A.Y., and S.G. designed the experimental and theoretical study, respectively; P.S.M. and S.G. jointly collaborated and led the experimental and theoretical parts, respectively; P.S.M. and S.N. performed the experimental research, and S.G. performed the theoretical research. S.G., P.S.M., P.S., and A.Y. jointly analyzed the results and wrote the Letter.

[1] T. Irifune, A. Kurio, S. Sakamoto, T. Inoue, and H. Sumiya, Nature (London) **421**, 599 (2003).

[2] S. H. Kirby, W. B. Durham, and L. A. Stern, Science **252**, 216 (1991).

[3] Y. Sun, F. Zhang, M. I. Mendelev, R. M. Wentzcovitch, and K.-M. Ho, Proc. Natl. Acad. Sci. USA **119**, e2113059119 (2022).

[4] D. A. Porter, K. E. Easterling, and M. Sherif, *Phase Transformations in Metals and Alloys*, 3rd ed. (CRC Press, 2009).

[5] H. Bhadeshia and R. Honeycombe, *Steels: Microstructure and Properties*, 3rd ed. (Butterworth-Heinemann, 2011).

[6] K. Otsuka and C. M. Wayman, *Shape Memory Materials*, 3rd ed. (Cambridge University Press, Cambridge, 1998).

[7] J. Wei, B. Feng, R. Ishikawa, T. Yokoi, K. Matsunaga, N. Shibata, and Y. Ikuhara, Nat. Mater. **20**, 951 (2021).

[8] J. A. Weiss, D. W. Oxtoby, D. G. Grier, and C. A. Murray, J. Chem. Phys. **103**, 1180 (1995).

[9] A. Yethiraj, A. Wouterse, B. Groh, and A. van Blaaderen, Phys. Rev. Lett. **92**, 058301 (2004).

[10] Y. Peng, F. Wang, Z. Wang, A. M. Alsayed, Z. Zhang, A. G. Yodh, and Y. Han, Nat. Mater. **14**, 101 (2015).

[11] P. S. Mohanty, S. Nöjd, M. J. Bergman, G. Nägele, S. Arrese-Igor, A. Alegria, R. Roa, P. Schurtenberger, and J. K. G. Dhont, Soft Matter **12**, 9705 (2016).

[12] M. J. Bergman, S. Nöjd, P. S. Mohanty, N. Boon, J. N. Immink, J. J. E. Maris, J. Stenhammar, and P. Schurtenberger, Soft Matter **17**, 10063 (2021).

[13] P. S. Mohanty, P. Bagheri, S. Nöjd, A. Yethiraj, and P. Schurtenberger, Phys. Rev. X **5**, 011030 (2015).

[14] S. Ganguly, P. S. Mohanty, P. Schurtenberger, S. Sengupta, and A. Yethiraj, Soft Matter **13**, 4689 (2017).

[15] M. C. Weinberg, D. P. Birnie and V. A. Shneidman, J. Non-Cryst. Solids **219**, 89 (1997).

[16] M. Avrami, J. Chem. Phys. **7**, 1103 (1939).

[17] M. Avrami, J. Chem. Phys. **8**, 212 (1940).

[18] M. Avrami, J. Chem. Phys. **9**, 177 (1941).

[19] R. Tao and J. M. Sun, Phys. Rev. Lett. **67**, 398 (1991).

[20] A.-P. Hynninen and M. Dijkstra, Phys. Rev. Lett. **94**, 138303 (2005).

[21] S. Nöjd, P. S. Mohanty, P. Bagheri, A. Yethiraj, and P. Schurtenberger, Soft Matter **9**, 9199 (2013).

[22] A. Yethiraj and A. van Blaaderen, Nature (London) **421**, 513 (2003).

[23] T. Colla, P. S. Mohanty, S. Nöjd, E. Bialik, A. Riede, P. Schurtenberger, and C. N. Likos, ACS Nano **12**, 4321 (2018).

[24] See Supplemental Material at http://link.aps.org/supplemental/10.1103/PhysRevMaterials.7.L080401 for a brief theoretical background and technical details on the experimental methods. The Supplemental Material also contains Refs. [30,31].

[25] M. Fanfoni and M. Tomellini, Nuovo Cimento D **20**, 1171 (1998).

[26] X. Liu, H. Li, and M. Zhan, Manufacturing Rev. **5**, 10 (2018).

[27] P. Tolédano and V. Dmitriev, *Reconstructive Phase Transitions* (World Scientific, 1996).

[28] S. Auer and D. Frenkel, Annu. Rev. Phys. Chem. **55**, 333 (2004).

[29] K. Binder, Rep. Prog. Phys. **50**, 783 (1987).

[30] M. J. Starink, J. Mater. Sci. **36**, 4433 (2001).

[31] A. Burbelko, E. Fraś, and W. Kapturkiewicz, Mater. Sci. Eng., A **413-414**, 429 (2005).

[32] S. Ganguly, S. Sengupta, P. Sollich, and M. Rao, Phys. Rev. E **87**, 042801 (2013).

[33] P. Nath, S. Ganguly, J. Horbach, P. Sollich, S. Karmakar, and S. Sengupta, Proc. Natl. Acad. Sci. USA **115**, E4322 (2018).

[34] S. Ganguly, S. Sengupta, and P. Sollich, Soft Matter **11**, 4517 (2015).

[35] P. Popli, S. Kayal, P. Sollich, and S. Sengupta, Phys. Rev. E **100**, 033002 (2019).

[36] A. Mitra, S. Ganguly, S. Sengupta, and P. Sollich, J. Stat. Mech. (2015) P06025.

[37] A. Zaccone and E. Scossa-Romano, Phys. Rev. B **83**, 184205 (2011).

[38] R. Milkus and A. Zaccone, Phys. Rev. B **93**, 094204 (2016).

[39] J. Krausser, R. Milkus, and A. Zaccone, Soft Matter **13**, 6079 (2017).

[40] C. L. Kelchner, S. J. Plimpton, and J. C. Hamilton, Phys. Rev. B **58**, 11085 (1998).

[41] D. Dube, N. Ahalawat, H. Khandelia, J. Mondal, and S. Sengupta, PLoS Comput. Biol. **15**, 1 (2019).

[42] P. M. Chaikin and T. C. Lubensky, *Principles of Condensed Matter Physics* (Cambridge University Press, 1995).

[43] P. Keim, G. Maret, U. Herz, and H. H. von Grünberg, Phys. Rev. Lett. **92**, 215504 (2004).

[44] L. Landau and E. Lifshitz, *Theory of Elasticity*, 3rd ed. (Pergamon Press, New York, 1986).

[45] S. Pronk and D. Frenkel, J. Phys. Chem. B **105**, 6722 (2001).

[46] S.-C. Lin, M. Oettel, J. M. Häring, R. Haussmann, M. Fuchs, and G. Kahl, Phys. Rev. Lett. **127**, 085501 (2021).

[47] S. Ganguly, G. P. Shrivastav, S.-C. Lin, J. Häring, R. Haussmann, G. Kahl, M. Oettel, and M. Fuchs, J. Chem. Phys. **156**, 064501 (2022).

[48] A. Jangizehi, F. Schmid, P. Besenius, K. Kremer, and S. Seiffert, Soft Matter **16**, 10809 (2020).